Next Materials 13 (2026) 102683

Contents lists available at ScienceDirect

Next Materials

journal homepage: www.sciencedirect.com/journal/next-materials

Research article

Comparative analysis of Titanium-doped zinc oxide (Ti-ZnO) nanophosphors synthesized via hydrothermal, Sol–Gel, and precipitation method

Mona Sri Santhakumar [a], Janna Ong Abdullah [b], Shafinaz Abd Gani [c], Zulkarami Berahim [d], Azzreena Mohamad Azzeme [c], Khairul Basyar Baharudin [a], Murni Halim [a,e], Rosfarizan Mohamad [a,e], Zulfazli M. Sobri [a,e,*]

[a] Department of Bioprocess Technology, Faculty of Biotechnology and Biomolecular Sciences, Universiti Putra Malaysia, Serdang, Selangor 43400 UPM, Malaysia
[b] Department of Cell and Molecular Biology, Faculty of Biotechnology and Biomolecular Sciences, Universiti Putra Malaysia, Serdang, Selangor 43400 UPM, Malaysia
[c] Department of Biochemistry, Faculty of Biotechnology and Biomolecular Sciences, Universiti Putra Malaysia, Serdang, Selangor 43400 UPM, Malaysia
[d] Institute of Tropical Agriculture and Food Security, Universiti Putra Malaysia, Serdang, Selangor, Malaysia
[e] Bioprocessing and Biomanufacturing Research Complex, Faculty of Biotechnology and Biomolecular Sciences, Universiti Putra Malaysia, Serdang, Selangor 43400 UPM, Malaysia

ARTICLE INFO

Keywords:
Titanium-doped zinc oxide nanophosphors
Hydrothermal synthesis
Sol gel synthesis
Co-precipitation
Physicochemical properties

ABSTRACT

Nanophosphors have attracted significant attention due to their tunable optical properties and potential photocatalytic applications. In this study, titanium-doped ZnO (Ti–ZnO) nanophosphors were synthesized via hydrothermal (H–TiZnO), sol–gel (S–TiZnO), and co-precipitation (P–TiZnO) methods to evaluate the effect of synthesis route on their structural and optical properties. UV–Vis spectra showed strong absorbance of H–TiZnO in the 250–400 nm region. Tauc plot analysis revealed synthesis-dependent optical bandgaps of 2.48 eV (P–TiZnO), 3.09 eV (H–TiZnO), and 4.71 eV (S–TiZnO), confirming the strong influence of preparation method. Photoluminescence spectra showed emission peaks at ~369 nm (H–TiZnO), ~396 nm (S–TiZnO), and ~402 nm (P–TiZnO), with H–TiZnO exhibiting the highest intensity, indicating improved optical quality. Dynamic light scattering results showed particle sizes of 377.47 ± 4.20 nm (H–TiZnO), 375.43 ± 1.52 nm (S–TiZnO), and 1049.67 ± 5.49 nm (P–TiZnO), while zeta potential analysis confirmed better colloidal stability for H–TiZnO. FTIR and XRD confirmed Zn–O/Ti–O bonding and the wurtzite ZnO structure with successful Ti incorporation. HRTEM and XPS further supported improved crystallinity and uniform morphology in H–TiZnO. Overall, hydrothermal synthesis produced Ti–ZnO nanophosphors with superior structural, optical, and stability properties, making them promise for optoelectronic and photocatalytic applications.

1. Introduction

Nanotechnology, the study and manipulation of materials at the nanoscale (1–100 nm), has emerged as one of the most transformative fields in modern science and engineering, offering unprecedented opportunities to design materials with highly specific and unable properties [1,2]. At the nanoscale, materials exhibit unique physicochemical characteristics that are markedly different from their bulk counterparts, including significantly enhanced surface area, quantum confinement effects, size-dependent optical and electronic behaviours, and increased chemical reactivity [3,4]. These distinctive features have opened new possibilities for creating materials with tailored functionalities for a wide range of applications. As a result, extensive research has been devoted to developing and exploring various nanomaterials such as metallic nanoparticles, semiconductor and metal oxide nanoparticles, polymer-based nanocomposites, and hybrid nanostructures [5,6].

Among the diverse array of functional nanomaterials, nanophosphors have emerged as a particularly promising class of luminescent materials that exhibit exceptional optical properties when engineered at the nanoscale. Nanophosphors are crystalline materials,

* Corresponding author at: Department of Bioprocess Technology, Faculty of Biotechnology and Biomolecular Sciences, Universiti Putra Malaysia, Serdang, Selangor 43400 UPM, Malaysia.
E-mail address: zulfazli@upm.edu.my (Z.M. Sobri).

https://doi.org/10.1016/j.nxmate.2026.102683
Received 2 April 2026; Received in revised form 19 June 2026; Accepted 29 June 2026
Available online 2 July 2026

typically consisting of a host lattice doped with activator ions (usually rare-earth or transition metal ions), that absorb energy and re-emit it as visible or near-infrared light through photoluminescence, electroluminescence, or cathodoluminescence mechanisms [7]. Various host materials, such as $ZnGa_2O_4$, can be doped with rare earth elements (REEs) like europium (Eu^{3+}), and terbium (Tb^{3+}) or various activators like Cr^{3+}, Co^{3+}, and Mn^{2+} to achieve different emission colours and functionalities [8].When synthesized at nanoscale dimensions, these phosphor materials demonstrate enhanced quantum efficiency, improved color purity, reduced light scattering, and superior dispersion properties compared to their conventional micrometer-sized counterparts. The unique size-dependent optical characteristics of nanophosphors, including quantum confinement effects and modified electronic band structures, have positioned them at the forefront of numerous technological applications. These include high-resolution display technologies (LEDs, OLEDs, and field emission displays), advanced bioimaging and biosensing platforms, solar energy conversion systems, solid-state lighting, anti-counterfeiting technologies, and radiation detection devices [9–11]. Recent advances in synthesis methodologies—such as sol-gel processing, hydrothermal synthesis, combustion methods, and microwave-assisted techniques—have enabled precise control over particle size, morphology, and surface chemistry, further expanding the functional capabilities of nanophosphors [12], which can be optimized through doping strategies and controlled synthesis [11,13]. As research intensifies in this domain, nanophosphors are increasingly recognized as essential building blocks for next-generation photonic devices and diagnostic tools, bridging the gap between fundamental nanoscience and practical technological innovation. Among these functional nanophosphor systems, metal oxide-based semiconductors such as ZnO have attracted particular attention due to their strong UV response and tunable optoelectronic properties through defect and doping engineering.

Titanium-doped zinc oxide (Ti-ZnO) nanophosphors have attracted considerable interest due to their enhanced optical, electrical, and antimicrobial properties. ZnO is a non-toxic, wide bandgap semiconductor that exhibits high optical transparency, good chemical stability, mechanical robustness, and strong nanoscale reactivity, making it a highly versatile material for a wide range of applications [14–16]. In addition, ZnO nanoparticles are widely used in biosensing and drug delivery systems due to their strong adsorption capability, high isoelectric point, surface-engineering potential, and photoconductive antimicrobial behaviour [17,18]. Furthermore, their properties can be effectively tuned through various doping strategies, including transition metal and rare earth element incorporation, enabling controlled modification of their electrical and optical behaviour. Such modifications have been reported to enhance performance in optoelectronic devices, photovoltaics, and sensor applications [19]. Doping ZnO with d-block elements such as Ti, Fe, Cu, Co, and Ni has been shown to significantly improve its physicochemical and optical properties [15,16,20,21]. Among these, Ti is particularly suitable due to the close ionic radius match between Ti^{4+} (0.68 Å) and Zn^{2+} (0.74 Å), as well as its multiple valence states (+2, +3, +4), which enhance chemical activity and defect engineering [22,23]. Recent studies have demonstrated that Ti incorporation into ZnO is an effective strategy for tailoring the optical and optoelectronic properties of the host material [24]. The substitution of Zn^{2+} by Ti^{4+} ions introduce localized electronic states and modifies the defect chemistry of ZnO, resulting in changes in charge-carrier concentration, optical absorption, and photoluminescence behaviour. These modifications enhance ultraviolet (UV) light sensitivity by promoting efficient generation and separation of photogenerated electron–hole pairs while suppressing charge recombination. Consequently, Ti doping enables fine-tuning of key optical parameters, including band-gap energy, absorption edge, and luminescence characteristics.

Although ZnO is widely studied for photocatalytic applications, its performance can be limited by structural instability. Titanium doping mitigates these limitations by improving lattice stability and optimizing defect states, thereby enhancing UV-light response and optical performance [25,26]. These improvements significantly expand the potential of Ti-ZnO for photocatalytic, sensing, and antimicrobial application [25,27]. Beyond single-element doping, multi-doping strategies have emerged as a promising approach for further enhancing ZnO performance. Co-doping with titanium and tin (Ti/Sn) has been reported to synergistically modify the electronic structure of ZnO, leading to enhanced UV photoresponse, improved crystallinity, reduced defect density, and controlled band-gap engineering [28,29]. The simultaneous incorporation of Ti and Sn ions influences the concentration of oxygen vacancies and zinc interstitials, which play key roles in determining luminescence efficiency, charge transport, and optical absorption characteristics. Such modifications contribute to improved photoconductivity, optical transparency, and photocatalytic activity. Furthermore, studies on Ti-doped and Ti/Sn co-doped ZnO synthesized via sol–gel processing have shown that controlled dopant incorporation can regulate particle growth, crystallite size, and surface morphology, thereby affecting light absorption and emission processes [29]. A microwave-assisted solvothermal study reported that Ti addition changed ZnO particle size, band gap, and degradation efficiency [26]. These findings highlight the importance of doping engineering as a versatile strategy for designing ZnO-based nanophosphors with tunable optical properties for UV sensing, photocatalysis, and advanced optoelectronic applications.

The synthesis method plays a critical role in the final properties of Ti-ZnO nanophosphors, and techniques such as sol–gel, hydrothermal, co-precipitation, and microwave-assisted synthesis are widely used to achieve uniform doping and controlled morphology [13–15,30,31]. The physicochemical properties of Ti-ZnO nanophosphors, including particle size, morphology, crystallinity, and optical characteristics, differ significantly across synthesis methods. Studies have shown that Ti incorporation modifies crystallinity, reduces structural defects, and enhances charge separation efficiency, leading to improved photocatalytic and biosensing performance [32–34]. However, excessive Ti doping can cause lattice distortions and reduced functionality, highlighting the need for an optimal doping concentration to achieve maximum performance [8].

Despite extensive research on Ti-doped ZnO nanomaterials, a clear research gap exists in the lack of systematic comparison of different synthesis methods on the structural, morphological, and optical properties of Ti-ZnO nanophosphors. Since synthesis routes strongly influence particle size, crystallinity, dopant distribution, defect concentration, and luminescence behavior, it remains unclear which preparation method yields the most optimized Ti-ZnO nanophosphors. Unlike previous reports that typically focus on a single synthesis route, this work provides a direct and controlled comparison of the structure–morphology–optical property relationships of Ti–ZnO nanophosphors synthesized via hydrothermal, sol–gel, and co-precipitation methods under identical conditions. The novelty of this study lies in this systematic comparative approach, which enables a reliable evaluation of how synthesis routes influence the physicochemical properties of Ti–ZnO nanophosphors. Accordingly, this study aims to synthesize and evaluate their physicochemical and optical properties using XRD, FTIR, UV–Vis, PL, zeta potential and particle size, HRTEM, and XPS. XPS analysis will be conducted on the selected best-performing sample to determine elemental composition and chemical states. The findings are expected to identify the most suitable synthesis method for producing Ti-ZnO nanophosphors with enhanced structural and optical properties.

2. Methodology

2.1. Synthesis of titanium-doped zinc oxide (Ti–ZnO) nanophosphors

I. **Hydrothermal method (H-TiZnO)**

Titanium-doped ZnO (3 mol% Ti) was synthesized using hydrothermal synthesis process from modified published

procedures [27,35,36]. A 0.1 M zinc nitrate solution (Chemiz, Malaysia) was mixed with 0.05 M titanium (IV) isopropoxide (97%, Sigma-Aldrich, USA) and magnetically stirred for 30 min at room temperature. The pH of the resulting solution was adjusted to approximately 11 by the dropwise addition of 3 M NaOH (Chemiz, Malaysia). The homogeneous mixture was then transferred into a Teflon-lined stainless-steel autoclave and subjected to hydrothermal treatment at 100 °C for 24 h. After natural cooling to room temperature, the obtained precipitate was vacuum filtered through a 0.22 μm PVDF membrane filter (47 mm diameter) and washed three times with a 1:1 (v/v) mixture of absolute ethanol (Chemiz, Malaysia) and distilled water to remove residual ions and organic impurities. The filtered product was dried at 80 °C for 18 h and subsequently calcined at 500 °C for 2 h with a heating rate of 5 °C min^{-1} .

II. **Sol–Gel method (S-TiZnO)**

Titanium-doped ZnO (3 mol% Ti) was synthesised by sol-gel method followed by [15,37,38] with slight modifications. A 0.1 M zinc nitrate solution (Chemiz, Malaysia) was mixed with 0.3 M citric acid as a chelating agent and stirred for 10 min. A 0.05 M titanium (IV) isopropoxide (97%, Sigma-Aldrich, USA) was then added to the solution and stirred for 30 min at room temperature. The pH of the resulting solution was adjusted to ~11 by the dropwise addition of 3 M NaOH (Chemiz, Malaysia). The solution was stirred at 60 °C for 2 h and subsequently aged at room temperature for 24 h to allow gel formation. The gel was dried overnight in an oven at 100 °C to form a xerogel, which was then calcined at 500 °C for 2 h, the heating rate was 5 °C·min^{-1}.

III. **Co-Precipitation Method (P-TiZnO)**

.

Titanium-doped ZnO (3 mol% Ti) was synthesized following the method reported in [39], with slight modifications. A 0.1 M zinc nitrate solution (Chemiz, Malaysia) was mixed with 0.05 M titanium (IV) isopropoxide (97%, Sigma-Aldrich, USA) and stirred for 30 min at room temperature. The pH of the solution was adjusted to ~11 by the dropwise addition of 3 M NaOH (Chemiz, Malaysia). The resulting mixture was stirred at 60 °C for 2 h and then left to stand for 1 h. The white precipitate formed was vacuum filtered using a 0.22 μm PVDF membrane filter (47 mm diameter) and washed three times with a 1:1 mixture of absolute ethanol (Chemiz, Malaysia) and distilled water. The filtered precipitate was dried at 80 °C for 18 h, followed by calcination at 500 °C for 2 h the heating rate was 5 °C·min^{-1}.

2.2. Characterization of Ti-ZnO nanophosphors

2.2.1. X-ray diffraction (XRD)

Powder X-ray diffraction (XRD) analysis was carried out using a Rigaku X-ray diffractometer (Model: SmartLab (2), MiniFlex 600) equipped with Cu Kα radiation (λ = 1.5406 Å). Diffraction patterns were collected over a 2θ range of 10°–80° at room temperature using a continuous scan mode. The obtained diffraction data were used for phase identification and structural analysis [40].

2.2.2. Fourier Transform Infrared (FTIR) spectroscopy

Fourier Transform Infrared (FTIR) spectra were recorded in the range of 500–4000 cm^{-1} using a PerkinElmer Spectrum 100 FTIR spectrometer. The samples were prepared using the standard KBr pellet method, and spectra were collected at room temperature with appropriate spectral resolution to identify bonding and functional groups [41].

2.2.3. UV–visible (UV–Vis) spectroscopy

Prior to optical measurements, the synthesized Ti–ZnO nanophosphors were dispersed in distilled water and sonicated for 30 min using an ultrasonic bath to obtain a homogeneous suspension and to minimize particle agglomeration. Ultraviolet–visible (UV–Vis) absorption spectra were recorded using a PerkinElmer Lambda 25 spectrophotometer in the wavelength range of 200–800 nm, with distilled water used as the baseline reference. All measurements were carried out at room temperature using quartz cuvettes with a 1 cm optical path length [33,42]. The optical band gap (Eg) of the Ti–ZnO nanophosphors was estimated using the Tauc relation. The absorption coefficient (α) was calculated from UV–Vis absorbance data, and Tauc plots of $(\alpha h\nu)^2$ versus photon energy ($h\nu$) were constructed assuming a direct allowed transition. The optical band gap was determined by extrapolating the linear portion of the plot to $(\alpha h\nu)^2 = 0$ [43].

2.2.4. Photoluminescence (PL) spectroscopy

Photoluminescence (PL) spectra were collected using a PerkinElmer LS−55 fluorescence spectrometer at room temperature. The excitation wavelength was fixed at 325 nm, and emission spectra were recorded over the appropriate wavelength range with standard slit widths and scan speeds as provided by the instrument software [44].

2.2.5. Hydrodynamic particle size (d, nm) and zeta potential (mV)

The hydrodynamic particle size (d, nm) and zeta potential of the Ti–ZnO suspensions were measured using a Malvern Zetasizer based on dynamic light scattering (DLS) and electrophoretic light scattering techniques, respectively. Prior to measurement, the samples were sonicated for 30 min in distilled water to obtain a well-dispersed suspension and minimize particle agglomeration and then diluted to avoid multiple scattering effects. All measurements were performed at room temperature, and the reported values represent the average of at least three independent measurements [45].

2.2.6. High-resolution transmission electron microscopy (HRTEM)

The morphology and microstructural features of the Ti–ZnO nanophosphors were examined using High-Resolution Transmission Electron Microscopy (HRTEM) (JEOL 1230, Japan). A small amount of the powdered sample was ultrasonically dispersed in distilled water, and a drop of the suspension was deposited onto a carbon-coated copper grid and allowed to dry under ambient conditions prior to imaging. HRTEM images were acquired at an accelerating voltage appropriate for high-resolution analysis [46,47].

2.2.7. X-ray photoelectron spectroscopy (XPS)

X-ray Photoelectron Spectroscopy (XPS) measurements were performed only for the best-performing sample using a Thermo Scientific X-ray Photoelectron Spectrometer. The analysis was conducted under ultra-high vacuum conditions using Al Kα radiation as the X-ray source. Survey spectra and high-resolution core-level spectra were collected for elemental and chemical state analysis, and all binding energies were calibrated with respect to the C 1 s peak at 284.8 eV [48]. The elemental atomic percentages obtained from XPS were used to calculate the Ti/Zn ratio using Ti/Zn = (atomic % Ti)/ (atomic % Zn).

2.3. Statistical analysis

Statistical analysis was performed using SPSS 16.0 (SPSS Inc., Chicago, IL, USA). Particle size, size distribution, and zeta potential data were analyzed by one-way ANOVA (Analysis of Variance) with post hoc Tukey's test applied for paired comparison of means.

3. Results & discussion

3.1. X-Ray diffractometer (XRD)

X-ray diffraction (XRD) is a fundamental technique for characterizing the crystalline structure, phase composition, and crystallite size of materials. By analyzing the diffraction patterns produced when X-rays interact with the crystal lattice, XRD provides insights into crystal

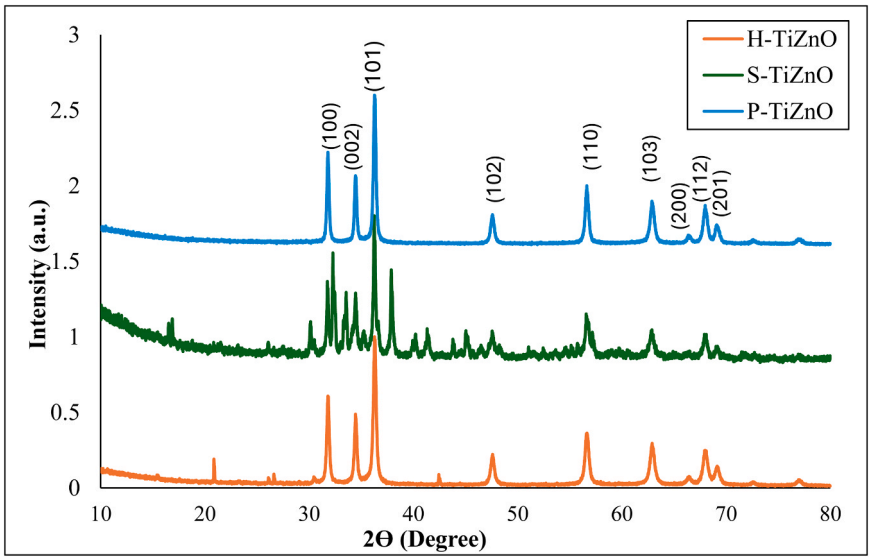

Fig. 1. XRD Spectra of Ti-ZnO nanophosphors.

Table 1
Structural parameters of Ti-doped ZnO nanophosphors calculated from the dominant (101) peak.

Sample	Peak position (2θ)	Max intensity	FWHM (°)	Crystallite size (nm)
H-TiZnO	36.28	12,109	0.42	19.9
S-TiZnO	36.24	3800	0.32	26.1
P-TiZnO	36.27	11,646	0.37	22.6

symmetry, lattice parameters, and structural defects [49]. This information is essential for understanding the effects of synthesis methods, doping, and post-treatment on material properties. The powder X-ray diffraction (XRD) spectra of Ti-doped ZnO nanophosphors synthesized via hydrothermal (H-TiZnO), sol–gel (S-TiZnO), and co-precipitation (P-TiZnO) routes are presented in Fig. 1. The XRD patterns of nanophosphors synthesized via hydrothermal, sol–gel, and co-precipitation routes confirm a single-phase hexagonal wurtzite ZnO structure, with no additional peaks corresponding to TiO_2 or other secondary phases. The most intense diffraction peaks in the 2θ range of 10°–80° correspond to the (100), (002), (101), (110), (103), and (112) planes, consistent with JCPDS file 01–079–0206 [26]. The patterns confirm the presence of the hexagonal wurtzite ZnO structure, with primary diffraction peaks observed at theta values of approximately 31.8°, 34.4°, and 36.3°, corresponding to the (100), (002), and (101) planes, respectively (JCPDS 01–079–0206). Based on Table 1 and a comparative analysis reveal that H-TiZnO possesses the highest peak intensity (12,109 counts), indicating a high degree of crystalline abundance and phase formation compared to S-TiZnO (3800 counts). However, the Full Width at Half Maximum (FWHM) of the dominant (101) peak was found to be 0.42° for H-TiZnO, 0.37° for P-TiZnO, and 0.32° for S-TiZnO. According to the

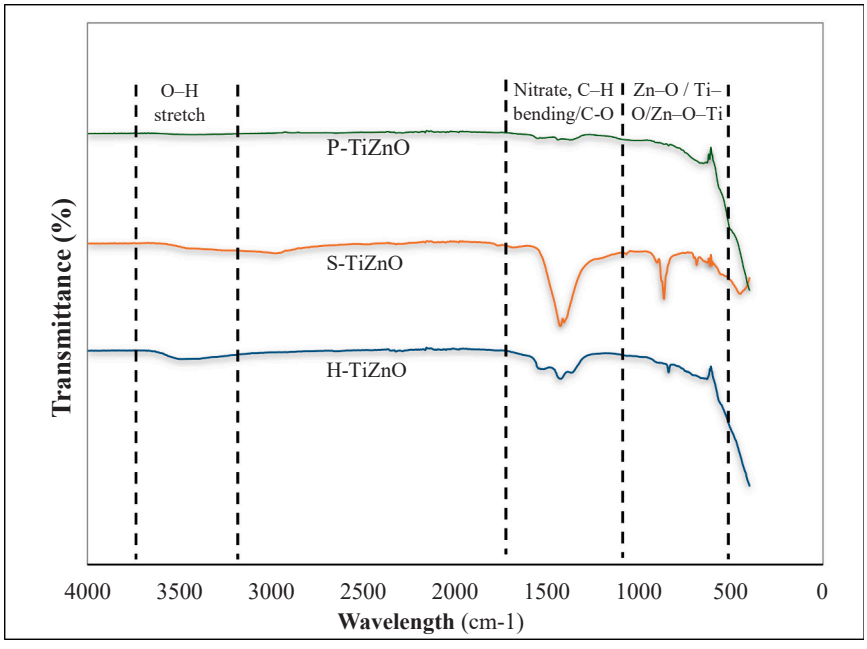

Fig. 2. FTIR Spectra of Ti-ZnO nanophosphors. Characteristic absorption bands correspond to O–H stretching, nitrate/C–H bending, C–O vibrations, and metal–oxygen modes (Zn–O, Ti–O, and Zn–O–Ti), confirming Ti incorporation into the ZnO lattice and the presence of surface functional groups.

Table 2
Reported FTIR spectral ranges from literature.

Assigned Functional Group	Wavenumber Range (cm^{-1})	Supporting Literature
O–H stretching (hydroxyl groups / adsorbed H_2O)	3600–3200	Kayiwa *et al.* (2021)
	3700–3584	Idress *et al.* (2019)
	3443	Irshad *et al.* (2024)
Nitrate	1420–1520	General range supported by literature
C–H bending / Carbonate group (CO_3^{2-})	1350–1470 (C–H bending)	FTIR Spectrum Table
	1380–1450 (CO_3^{2-})	Tan *et al.* (2020)
Zn–O / Ti–O/Zn–O–Ti vibrations	400–600	Sarathi *et al.* (2022)
	800–1050	Irshad *et al.* (2024)

Scherrer equation, these values correspond to average crystallite sizes of approximately 19.9 nm, 22.6 nm, and 26.1 nm, respectively. While S-TiZnO exhibits the narrowest (sharpest) peaks, its significantly lower intensity suggests a lower overall crystalline volume or the presence of amorphous regions. In contrast, H-TiZnO and P-TiZnO demonstrate superior crystal growth and structural stability. Small secondary reflections observed in the H-TiZnO sample at low angles suggest trace amounts of secondary phases, whereas P-TiZnO displays the highest phase purity. The enhanced diffraction intensity in H-TiZnO suggests improved crystallinity and better long-range structural ordering, which may contribute to enhanced photoluminescence efficiency typically observed in hydrothermally synthesized ZnO-based nanomaterials [50]. This trend is consistent with previous reports that hydrothermal synthesis generally produces better-crystallized ZnO-based nanostructures than sol–gel or co-precipitation methods, due to slower crystal growth and improved lattice ordering [5]. The superior crystallinity of H-TiZnO is associated with improved structural ordering, which can facilitate radiative recombination processes and is consistent with the higher photoluminescence intensity observed for this sample compared with S-TiZnO and P-TiZnO, in agreement with previous studies on doped ZnO nanomaterials [7,38].

3.2. Fourier Transform Infrared (FTIR) Spectra

Fourier-transform infrared (FTIR) spectroscopy is a widely used technique for identifying chemical bonds and functional groups in materials by measuring their characteristic vibrational modes. FTIR provides information on the molecular composition, surface chemistry, and possible interactions between dopants and the host matrix. It is particularly useful for confirming the presence of hydroxyl groups,

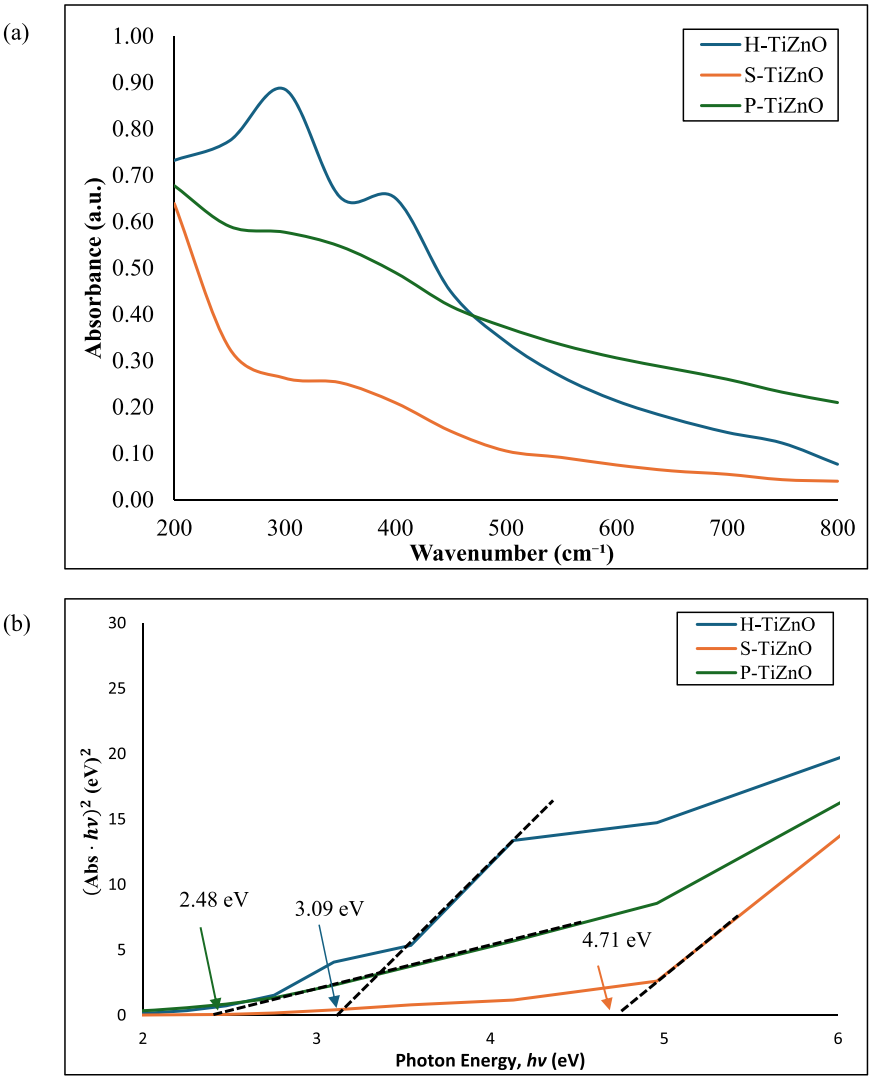

Fig. 3. (a) UV–Vis absorption spectra of H–TiZnO, S–TiZnO, and P–TiZnO nanophosphors recorded in the wavelength range of 200–800 nm, and (b) Tauc plots of $(\alpha h\nu)^2$ versus photon energy ($h\nu$) used for bandgap estimation of the corresponding samples.

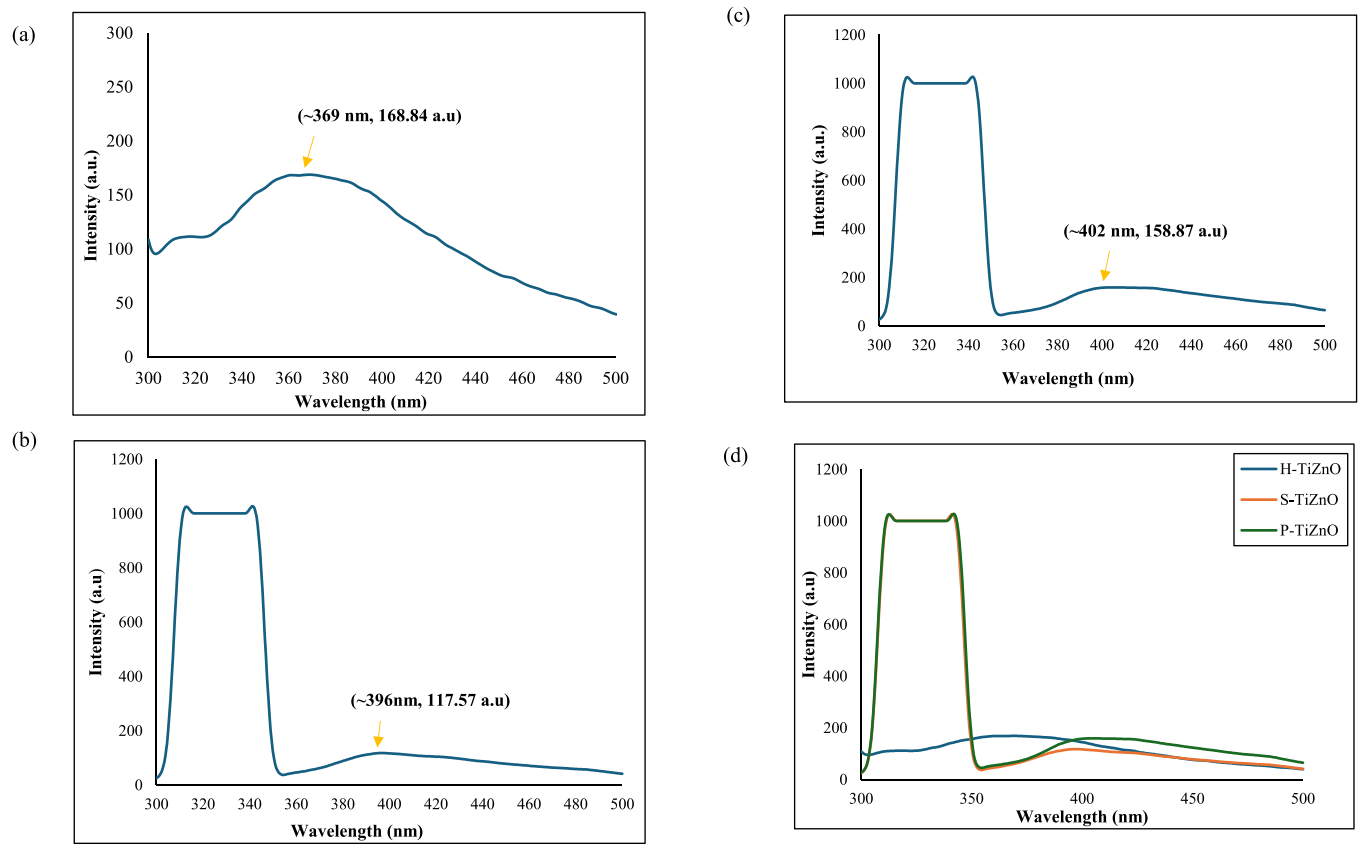

Fig. 4. Photoluminescence (PL) spectra of (a) H-TiZnO, (b) S-TiZnO, and (c) P-TiZnO nanophosphors under 325 nm excitation, and (d) comparative PL spectra of H-TiZnO, S-TiZnO, and P-TiZnO nanophosphors.

metal–oxygen bonds, and organic residues, offering insights into material structure, purity, and surface modification [51]. The FTIR spectra of the Ti-doped ZnO nanophosphors synthesized by hydrothermal, sol–gel and co-precipitation routes exhibit several characteristic vibrational modes that confirm both the oxide framework and the presence of surface species. Fig. 2 presents the FTIR spectra of the three samples, highlighting the functional groups identified based on the corresponding wavelength ranges, Table 2, and previously reported FTIR data from the literature. A broad band in the 3600–3200 cm^{-1} region is assigned to O–H stretching from surface hydroxyl groups and adsorbed water, in agreement with reported values for ZnO-based nanomaterials [20,52,53]. Absorptions between about 1420–1520 cm^{-1} are attributed to nitrate groups originating from metal–nitrate precursors [20,53,54], whereas features in the 1350–1470 cm^{-1} region, with a component around 1380–1450 cm^{-1} , correspond to overlapping C–H bending [55] and carbonate (CO_3^{2-}) vibrations [20,36,56], consistent with earlier FTIR studies of ZnO prepared from nitrate and organic routes [22]. In the low-wavenumber region, strong bands in the 400–600 cm^{-1} range are characteristic of Zn–O lattice vibrations [14,54,55] while additional modes between 800–1050 cm^{-1} are associated with Ti–O and mixed Zn–O–Ti stretching, supporting successful incorporation of Ti into the ZnO lattice [48,56] rather than formation of a separate TiO_2 phase [53], as also observed in previous investigations of Ti-doped ZnO systems. FTIR analysis of the three Ti-doped ZnO samples shows that S-TiZnO has the sharpest and most defined peaks, indicating well-resolved surface functional groups, while H-TiZnO exhibits strong Zn–O and Ti–O–Zn vibrations with fewer impurity-related peaks, reflecting higher lattice purity. Therefore, S-TiZnO provides better peak clarity, whereas H-TiZnO demonstrates superior structural quality.

3.3. *UV-visible spectroscopy*

UV–visible spectroscopy is a credible technique that plays a crucial role in the study and primary characterization of synthesized nanoparticles [57]. The UV–Vis absorption profiles of Ti-doped ZnO nanophosphors synthesized via hydrothermal, sol–gel, and co-precipitation routes demonstrate a clear dependence of optical behaviour on the preparation method shown in Fig. 3(a). The hydrothermal sample (H–TiZnO) shows strong absorption in the 250–350 nm region, corresponding to dominant band-edge transitions of ZnO, along with a broadened shoulder extending into the 350–400 nm region, which may be attributed to defect-related states such as oxygen vacancies [50,58]. The co-precipitated sample (P–TiZnO) exhibits an absorption peak centred around ~300 nm, indicating pronounced band-to-band transitions and relatively well-preserved band-edge characteristics. Conversely, the sol–gel sample (S–TiZnO) displays a dominant absorption feature at approximately 550 nm, sub-bandgap defect-related states, suggesting a higher density of localized electronic states compared with the other samples [7]. Thus, these results indicate that the hydrothermal method provides a balanced optical response with both band-edge absorption and controlled defect states, whereas the co-precipitation method favours stronger band-to-band transitions and the sol–gel method introduces more pronounced defect-related absorption features [33].

A Tauc plot is essential because it provides a quantitative method to determine the optical bandgap by linearizing absorption data and enabling accurate extrapolation of the bandgap energy [59,60]. As shown in Fig. 3(b), the optical bandgap of TiZnO significantly varies with the synthesis route. P-TiZnO exhibits the lowest bandgap (2.48 eV), indicating enhanced absorption of lower-energy photons and improved suitability for visible-light-driven applications. H-TiZnO shows an intermediate bandgap (3.09 eV), reflecting moderate optical activity,

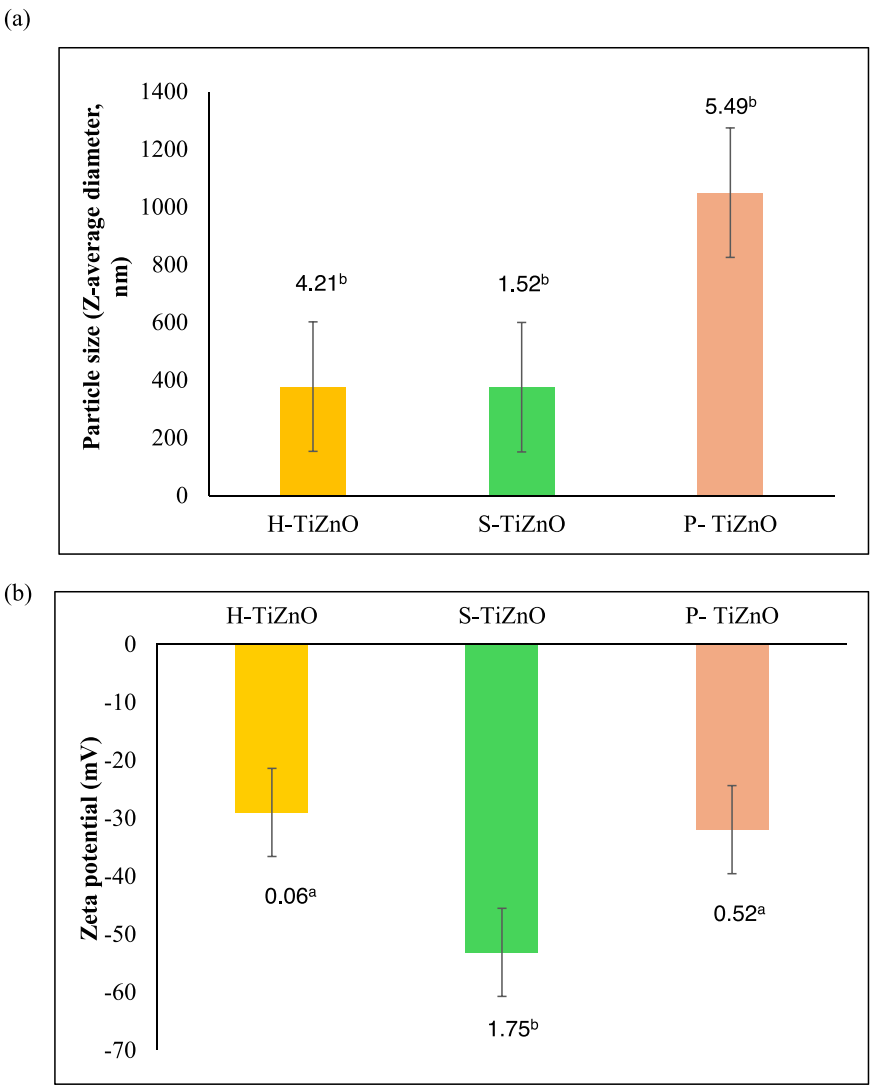

Fig. 5. Z-average particle size (nm) (a) and zeta potential (mV) (b) of Ti-ZnO nanophosphors prepared by three methods. Data are presented as mean ± SE (n = 3). Different superscript letters indicate significant differences ($p < 0.05$, ANOVA, Tukey's test).

while S-TiZnO presents the highest bandgap (4.71 eV), requiring higher photon energy for electronic excitation. This trend confirms that the synthesis method strongly influences the electronic structure of TiZnO, likely due to variations in crystallinity, defect states, particle size, or phase composition [60–62].

3.4. Photoluminescence (PL) spectra

Photoluminescence (PL) is a non-destructive, contactless optical technique used to probe the electronic structure of materials by analyzing light emitted after photoexcitation. Unlike absorption spectroscopy, which measures transitions from ground to excited states, PL examines radiative transitions from excited states back to the ground state, providing insight into electronic structure, defect states, and luminescence properties. Excitation spectra, like absorption spectra, indicate the wavelengths at which materials efficiently absorb energy to produce emission [63]. Crystallinity is strongly correlated with PL behaviour, where a highly crystalline structure reduces defect-mediated non-radiative recombination, resulting in stronger radiative emission. In contrast, lower crystallinity introduces structural disorder that can reduce emission intensity and slightly shift the emission wavelength [64, 65]. Photoluminescence (PL) spectra of the Ti-doped ZnO samples under 325 nm excitation are presented in Fig. 4. The H-TiZnO sample (Fig. 4a) exhibits a sharp near-band-edge (NBE) emission peak at approximately 369 nm with the highest intensity (168.84 a.u), indicating superior crystallinity and efficient excitonic radiative recombination with minimal non-radiative losses [33,66]. In comparison, the S-TiZnO sample (Fig. 4b) exhibits a redshifted emission peak at ~396 nm with reduced intensity (117.57 a.u), suggesting increased structural disorder that may enhance non-radiative recombination processes [67]. Similarly, the P-TiZnO sample (Fig. 4c) shows a further redshifted peak at ~402 nm with intermediate intensity (158.87 a.u), which may be attributed to variations in crystal growth dynamics and Ti incorporation during synthesis, influencing the local electronic structure This confirms that the synthesis route plays a key role in tailoring the optical properties of Ti-doped ZnO through its influence on crystallinity and emission behaviour. The comparative PL analysis (Fig. 4d) further shows that the hydrothermal-synthesised sample exhibits the strongest dominant emission, indicating superior structural quality compared to the other synthesis routes, which aligns with previous reports that hydrothermal synthesis generally yields nanocrystals with good crystallinity and purity [17,31].

3.5. Hydrodynamic particle size (d, nm) and Zeta potential (mV)

Dynamic light scattering (DLS) particle size, expressed as the Z-

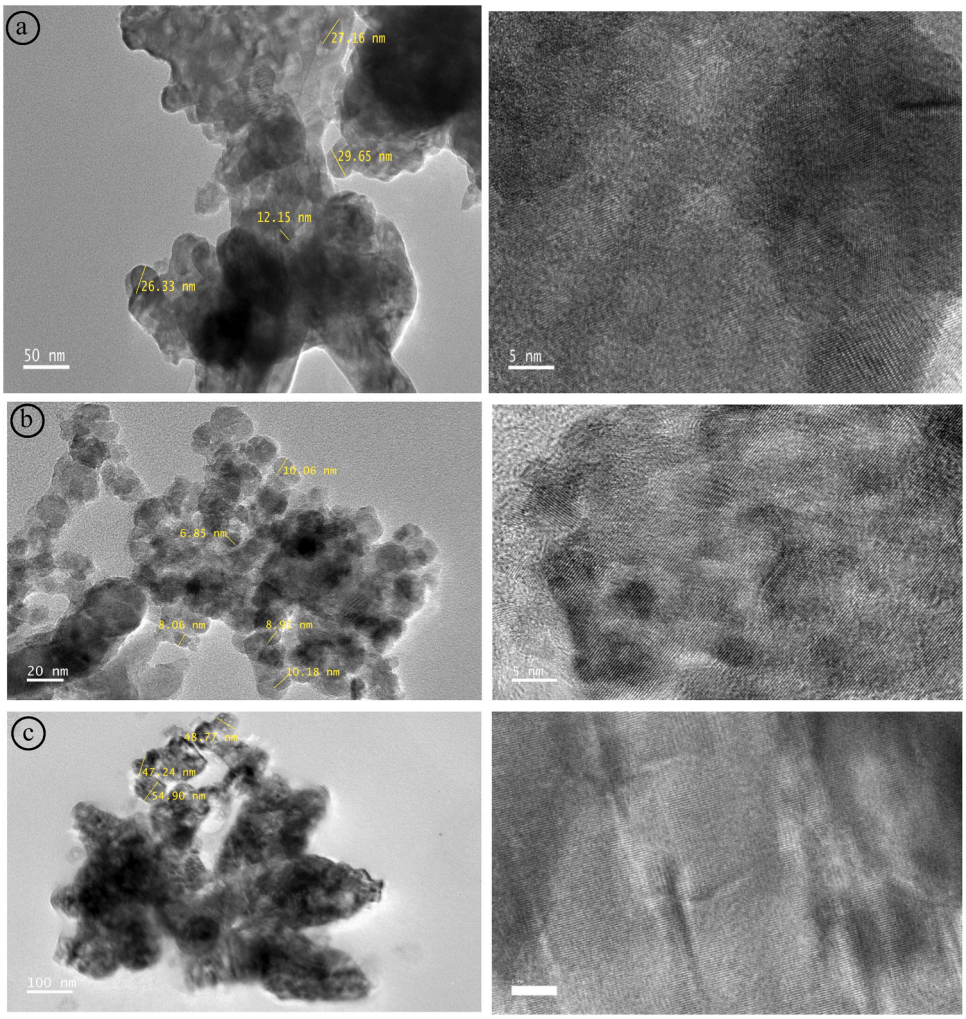

Fig. 6. HR-TEM image (left) and lattice fringes (right) of Ti-ZnO nanophosphors, (a) hydrothermal (H-TiZnO), (b) sol–gel (S-TiZnO), and (c) co-precipitation (P-TiZnO).

average diameter, measures the hydrodynamic size of GQDs, including the nanoparticle core together with any associated solvent layer, polymer coating, or surface-bound molecules [68,69], whereas zeta potential (mV) is a key indicator of the surface charge and colloidal stability of nanoparticles in suspension [70,71]. It reflects the potential difference between the dispersion medium, and the stationary layer of fluid attached to the particle surface, providing insight into electrostatic interactions, aggregation tendencies, and surface reactivity. Materials with high absolute zeta potential (positive or negative) are generally more stable due to stronger electrostatic repulsion, whereas low zeta potential values often lead to particle aggregation and reduced dispersion stability [71,72]. Fig. 5 illustrates the particle size distribution (a) zeta potential (b) and of the Ti-doped ZnO nanophosphors, revealing notable differences among the samples. All nanophosphors exhibited a positive surface charge at the measurement pH, suggesting the presence of protonated surface groups. Dynamic light scattering analysis showed that H-TiZnO and S-TiZnO had similar Z-average particle sizes of 377.47 ± 4.21 nm and 375.43 ± 1.52 nm, respectively, indicating uniform dispersion. In contrast, P-TiZnO exhibited a markedly larger hydrodynamic diameter of 1049.67 ± 5.49 nm, likely due to particle aggregation. Zeta potential analysis further demonstrated that S-TiZnO possessed the highest negative surface charge (-53.13 ± 1.75 mV), reflecting superior colloidal stability. H-TiZnO and P-TiZnO, with zeta potentials of -29.00 ± 0.06 mV and -31.97 ± 0.52 mV, respectively, showed moderate stability, suggesting a higher tendency for aggregation under similar conditions.

These results indicate that both surface charge and particle size are key determinants of colloidal behaviour, with S-TiZnO being the most stable dispersion among the tested nanophosphors. These relatively low magnitudes (< 10 mV) indicate limited electrostatic stabilization and help explain the large hydrodynamic diameters observed, especially for the co-precipitated sample, which likely consists of loosely aggregated primary particles [3,6]. In line with previous reports on ZnO and doped ZnO, the higher zeta potential of the co-precipitated powder can be ascribed to a freshly formed, highly hydroxylated and largely organic-free surface that favours protonation, whereas the lower value for the sol–gel product reflects partial coverage by residual organic species and extensive condensation of surface –OH groups, which screen or reduce the number of protonatable sites [6,30]. The intermediate zeta potential of the hydrothermally synthesized sample is consistent with literature showing that elevated temperature and pressure promote crystallite growth and partial surface sintering, decreasing hydroxyl density but maintaining a relatively clean, crystalline surface. This zeta potential results revealed that the co-precipitation route yields Ti-ZnO with the most reactive, strongly charged surface, the sol–gel route produces more passivated particles with weaker electrostatic interactions, and the hydrothermal method offers a balance between surface charge and structural order, which should be considered when selecting materials for photocatalytic, optical, or biological applications.

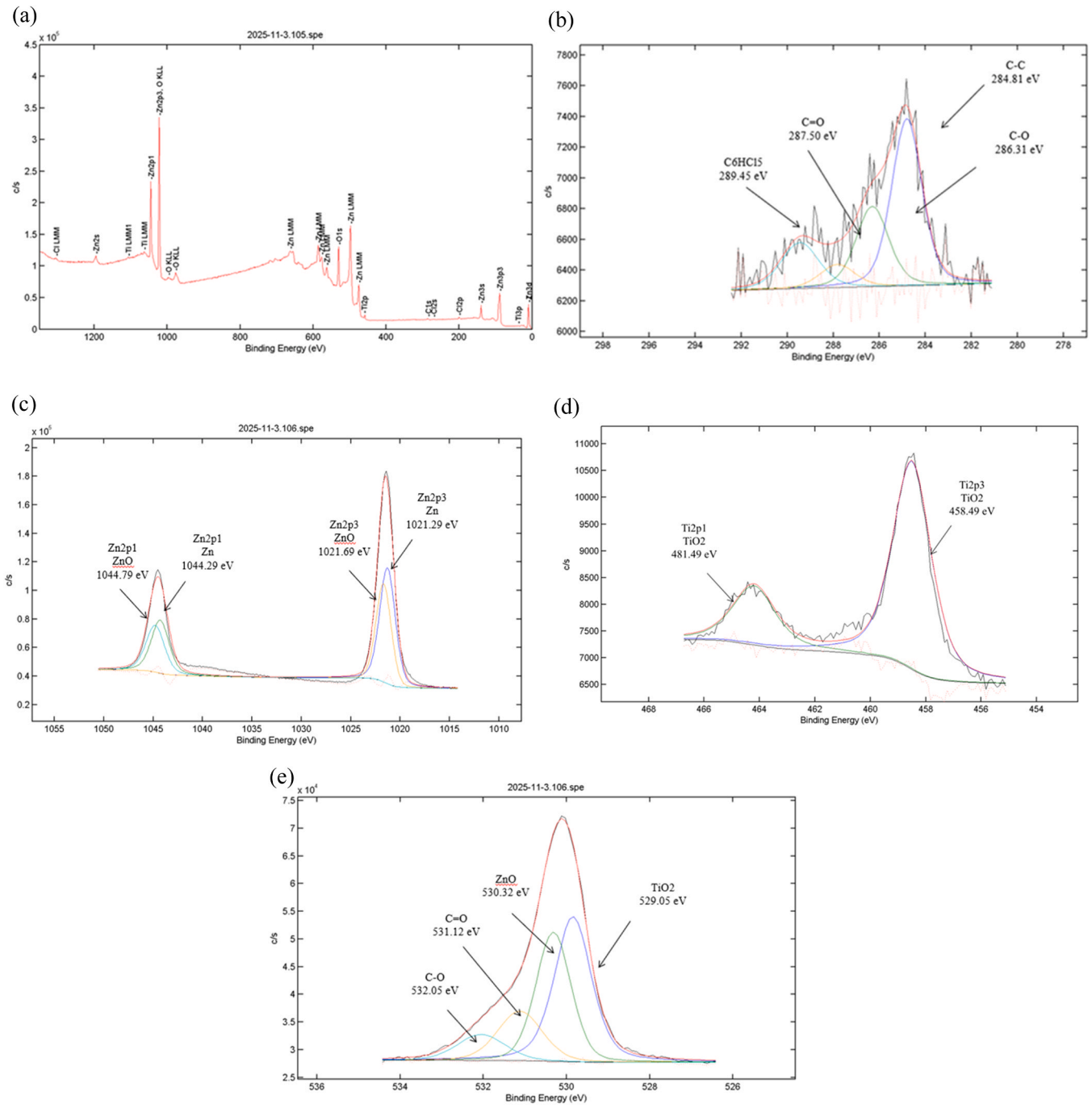

Fig. 7. XPS spectra of H–TiZnO nanophosphors. (a) Wide survey scan indicating the presence of Zn, Ti, O, and C on the sample surface. High-resolution core-level spectra for (b) C 1 s, showing adventitious carbon and bonding states; (c) Zn 2*p*, showing the $2p_{3/2}$ and $2p_{1/2}$ spin-orbit doublets; (d) Ti 2*p*, indicating the Ti^{4+} oxidation state; and (e) O 1 s, deconvoluted into lattice oxygen (O_L) and surface-adsorbed oxygen (O_S) components.

3.6. High-resolution transmission electron microscopy (HRTEM)

High-resolution transmission electron microscopy (HRTEM) is a powerful imaging technique for studying materials at the atomic scale, providing direct visualization of morphology, lattice fringes, and defects. Unlike diffraction methods, which average over large regions, HRTEM reveals local structural information, making it particularly useful for non-crystalline or defect-containing crystals. Care must be taken in interpreting HRTEM images, as dynamical and nonlinear effects can distort projections, especially in thicker samples, so thin specimens are preferred [73]. HRTEM analysis revealed distinct differences in particle morphology and crystallinity among the Ti-ZnO nanophosphors synthesized using hydrothermal, sol–gel, and co-precipitation routes as shown in Fig. 6. The hydrothermal method produced aggregated but well-defined nanocrystals with particle sizes in the range of 12–30 nm, exhibiting sharp and continuous lattice fringes that confirm high crystallinity with minimal internal strain. These features suggest the formation of well-ordered crystal domains and reduced density of non-radiative centers, which is desirable for enhancing luminescence efficiency [74]. In contrast, the sol–gel–derived Ti-ZnO showed heavily aggregated, ultra-small nanoparticles approximately 12–30 nm with fragmented and less distinct lattice fringes, indicating a polycrystalline structure with higher internal strain and numerous lattice defects [31]. The co-precipitation samples formed larger approximately 47–54 nm,

Table 3
XPS elemental composition and chemical state distribution of the sample.

Element	Atomic %	Weight %	Compound / Chemical State	Contribution (%)
C	4.56	1.40	C–C	49.32
			C–O	25.80
			C═O	7.91
			C_6HCl_5	16.96
O	46.56	19.01	TiO_2	42.19
			ZnO	32.74
			C═O	16.04
			C–O	9.03
Cl	1.78	1.61	–	–
Ti	1.41	1.72	TiO_2	100.00
Zn	45.69	76.25	Zn (metallic)	54.84
			ZnO	45.16

irregular clusters but still displayed visible parallel fringes, confirming crystallinity; however, their broader and less uniform fringes imply lower structural ordering compared to the hydrothermal product. Overall, the hydrothermal method yielded Ti-ZnO nanophosphors with superior crystalline quality and optimal particle size, aligning with previous reports that highlight hydrothermal synthesis as an effective route for producing defect-reduced, highly crystalline metal oxide nanostructures suitable for luminescent applications [7].

3.7. X-Ray photoelectron spectra (XPS)

X-ray photoelectron spectroscopy (XPS) is a surface-sensitive analytical technique used to determine the elemental composition, chemical states, and electronic structure of materials. By measuring the binding energies of core electrons, XPS reveals information on oxidation states, dopant incorporation, and surface chemical environments. This technique is essential for understanding surface chemistry and the interactions between dopants and the host material [75]. The XPS survey scan (Fig. 7(a) and Table 3) confirms the presence of C, O, Cl, Ti, and Zn in H-TiZnO sample, with oxygen (46.56 at%) and zinc (45.69 at%) being the dominant surface elements, indicating that the material is mainly composed of zinc oxide–based species. The high-resolution C 1 s spectrum (Fig. 7(b) and Table 3) further reveals four main carbon bonding states: C–C at 284.81 eV (49.32%), C–O at 286.31 eV (25.80%), C═O at 287.50 eV (7.91%), and a high-binding-energy C_6HCl_5 component at 289.45 eV (16.96%), confirming the presence of oxygenated functional groups and trace chlorinated carbon species, consistent with the chlorine detected in the survey scan [76,77]. Meanwhile, the high-resolution Zn 2*p* spectrum (Figure7 (c) and Table 3) shows distinct peaks for both metallic Zn (Zn $2p_{3/2}$ at 1021.29 eV and Zn $2p_{1/2}$ at 1044.29 eV) and ZnO (Zn $2p_{3/2}$ at 1021.69 eV and Zn $2p_{1/2}$ at 1044.79 eV), with the quantification indicating 54.84% metallic Zn and 45.16% ZnO [78]. The Ti 2*p* spectrum (Figure7 (d) and Table 3) shows Ti $2p_{3/2}$ and Ti $2p_{1/2}$ peaks at 458.49 eV and 481.49 eV, confirming the presence of Ti^{4+} in TiO_2. The absence of Ti^{3+} or Ti^{2+} features indicates that titanium exists exclusively in its fully oxidized state, with quantitative fitting showing 100% TiO_2, reflecting high chemical stability [79]. O 1 s quantitative analysis (Fig. 7(e) and Table 3) reveals multiple chemical environments, including lattice oxygen associated with Zn–O (32.74%), Ti–O-related oxygen species (42.19%), and surface oxygen-containing groups attributed to C═O (16.04%) and C–O (9.03%) species from adsorbed oxygenated carbon contaminants. These results indicate the coexistence of lattice oxygen and surface-related oxygen functionalities within the samples. Therefore, the O 1 s deconvolution confirms a ZnO-based structure with Ti–O chemical interactions and surface defect-related states, in good agreement with the single-phase XRD analysis. [80]. Taken together, the experimental Ti/Zn ratio (0.031), corresponding to approximately 3 at% Ti, is in good agreement with the theoretical doping level, confirming successful Ti incorporation into the ZnO.

4. Conclusion

In conclusion, the comparative analysis of Ti-doped ZnO nanophosphors synthesized via hydrothermal, sol–gel, and co-precipitation methods demonstrates that the synthesis route strongly influences their structural, optical, and stability-related properties. A quantitative comparison of these properties is summarized in Table 4. Among all samples, H–TiZnO exhibited superior overall performance, as evidenced by XRD, optical, and morphological analyses showing higher crystallinity, improved optical response, and enhanced structural ordering within a single-phase hexagonal wurtzite ZnO structure. FTIR analysis confirmed the presence of characteristic metal–oxygen vibrational modes (Zn–O and Ti–O-related bonds), indicating successful incorporation of titanium into the ZnO matrix and the formation of a stable metal–oxygen framework. UV–Vis spectroscopy showed enhanced absorption in the 250–400 nm region. Photoluminescence spectra exhibited an emission peak at ~369 nm for H–TiZnO.The hydrothermal sample (H–TiZnO) exhibited moderate colloidal stability (−29 mV), whereas the sol–gel sample showed superior stability (−53.13 mV) due to stronger electrostatic repulsion. However, despite its lower zeta potential, the hydrothermal sample demonstrated better overall crystallinity, optical response, and defect suppression, making it more effective for enhancing the structural and optoelectronic performance of Ti-doped ZnO nanophosphors. HRTEM analysis further revealed a more homogeneous morphology with fewer structural imperfections. XPS confirmed Zn^{2+}, Ti^{4+} with Ti–O bonding, and minor Zn^{0}-like surface states, while O 1 s revealed Zn–O, Ti–O, and surface oxygen species, consistent with a ZnO-based structure in agreement with XRD results. Thus, these results demonstrate that hydrothermal synthesis is the most effective method for producing highly crystalline, optically active, and

Table 4
Quantitative comparison of structural, optical, and stability properties of Ti-doped ZnO nanophosphors synthesized via hydrothermal, sol–gel, and co-precipitation methods.

Characterization	Criterion	Hydrothermal (H–TiZnO)	Sol–gel (S–TiZnO)	Co-precipitation (P–TiZnO)
X-ray diffraction (XRD)	Sharp XRD peaks indicate high crystallinity	High crystallinity, sharp peaks	Broader peaks, less ordered	Moderate crystallinity
Fourier-transform infrared (FTIR)	Zn–O at 400–600 cm^{-1} , Ti–O at 500–700 cm^{-1} , no organics > 1000 cm^{-1} indicates high purity	Cleaner surface / high purity	Organic residue / poor purity	Minimal residue / moderate purity
UV–Vis spectroscopy	Absorption edge ~375–380 nm; Eg from Tauc plot (~3.3 eV for ZnO benchmark)	Eg = 3.09 eV	Eg = 4.71 eV	Eg = 2.48 eV
Photoluminescence (PL)	NBE emission ~360–380 nm; defect emission ~400–650 nm	~369 nm (strong intensity)	~396 nm (moderate intensity)	~402 nm (lower intensity)
Hydrodynamic Particle size (d.nm)	Particle sizes < 500 nm favour good dispersion	377.47	375.43	1049.67
Zeta potential (mV)	≥ 30 mV indicates good colloidal stability	−29.00	−53.13	−31.97
High-resolution TEM (HRTEM)	Primary particle size < 20 nm desirable for high surface area; uniform morphology	~12–30 nm	~6–10 nm	~47–54 nm

structurally stable Ti-doped ZnO nanophosphors for photonic and optoelectronic applications.

CRediT authorship contribution statement

Zulfazli M. Sobri: Visualization, Validation, Supervision, Project administration, Investigation, Funding acquisition, Data curation, Conceptualization. **Azzreena Mohamad Azzeme:** Visualization, Validation, Supervision, Investigation. **Khairul Basyar Baharudin:** Validation, Supervision, Investigation. **Murni Halim:** Visualization, Validation, Supervision. **Rosfarizan Mohamad:** Visualization, Validation, Supervision. **Mona Sri Santhakumar:** Writing – review & editing, Writing – original draft, Visualization, Methodology, Data curation, Conceptualization. **Janna Ong Abdullah:** Validation, Supervision, Investigation. **Shafinaz Abd Gani:** Visualization, Validation, Supervision, Data curation. **Zulkarami Berahim:** Validation, Supervision, Investigation.

Ethics declaration

Not applicable.

Clinical trial registration

This study is not a clinical trial; therefore, registration is not applicable.

Consent to publish

Not applicable.

Consent to participate

Not applicable.

Funding

This work was supported by Geran Putra Siswazah (UPM. RMC.800–2/1/2025/GP-IPS/9819700) and Geran Putra (UPM. RMC.800–3/3/1/2024/FASTTRACK/9790500), financed by Universiti Putra Malaysia. This project belongs to the Bioprocessing & Biomanufacturing University Driven Research Program (UDRP), Universiti Putra Malaysia.

Declaration of Competing Interest

The authors declare that they have no known competing financial interests or personal relationships that could have appeared to influence the work reported in this paper.

Acknowledgements

The authors thank Universiti Putra Malaysia for support and resources provided for this study.

References

[1] S. Bayda, M. Adeel, T. Tuccinardi, et al., The history of nanoscience and nanotechnology: from chemical-physical applications to nanomedicine, Molecules 25 (2020), https://doi.org/10.3390/molecules25010112.
[2] R. Tomar, Overv. Appl. Nanotechnol. (2023) 1–26.
[3] K.S. Suhas, V.K. Reddy, T. Reddy, et al., A comprehensive review on nanoparticles: classification, properties, and mechanical effects, Epub ahead of print 29, Discov. Mater. (November 2025), https://doi.org/10.1007/s43939-025-00455-9. Epub ahead of print 29.
[4] W.N.Z. Wan Azamuddin, J.O. Abdullah, A. Mohamad Azzeme, et al., A multidimensional review of the applications and implications of quantum dots in modern agriculture, Discov. Mater. 5 (1) (December 2025), https://doi.org/10.1007/s43939-025-00403-7.
[5] M.A. Darwish, W. Abd-Elaziem, A. Elsheikh, et al., Advancements in nanomaterials for nanosensors: a comprehensive review, Nanoscale Adv. 6 (2024) 4015–4046.
[6] Y. Khan, H. Sadia, S.Z. Ali Shah, et al., Classification, synthetic, and characterization approaches to nanoparticles, and their applications in various fields of nanotechnology: a review, Catalysts 12 (November 2022), https://doi.org/10.3390/catal12111386.
[7] R. Kubrin, Nanophosphor coatings: technology and applications, opportunities and challenges, KONA Powder Part. J. 31 (2014) 22–52.
[8] M.I. Chen, A.K. Singh, J.L. Chiang, et al., Zinc gallium oxide—a review from synthesis to applications, Nanomaterials 10 (2020) 1–37.
[9] V. Kumar, O.M. Ntwaeaborwa, T. Soga, et al., Rare earth doped zinc oxide nanophosphor powder: a future material for solid state lighting and solar cells, ACS Photonics 4 (2017) 2613–2637.
[10] P.K. Upadhyay, N. Sharma, S. Sharma, et al., Photo and thermoluminescence of Eu doped ZnO nanophosphors, Journal Materials Science Materials Electronics 32 (2021) 17080–17093.
[11] U. Mushtaq, I. Ayoub, V. Kumar, et al., Persistent luminescent nanophosphors for applications in cancer theranostics, biomedical, imaging and security, Mater. Today Bio 23 (December 2023), https://doi.org/10.1016/j.mtbio.2023.100860.
[12] M. Farooq, H. Rafiq, A. ul I. Shah, et al., Review— On the Development of Phosphors for Luminescent Materials: Synthesis, Characterization, Applications and Evolution of Phosphors as White-Light-Emitting Diodes, ECS J. Solid. State Sci. Technol. 12 (2023) 126002.
[13] J. Kumar, I. Roy, Upconverting nanophosphors for various sensing applications, Talanta Open. 9 (August 2024), https://doi.org/10.1016/j.talo.2024.100302.
[14] S. Pauline G, S K. Properties of Ti doped ZnO nanoparticles under solid state reaction method involving vacuum annealing, 5, Phys. B Condens. Matter 649 (January 2023), https://doi.org/10.1016/j.physb.2022.414409, 5.
[15] K. Srinivas, S. Verma, B.T. Rao, et al., Ti doped ZnO nanoparticles for photocatalytic hydroxyl radical generation under UV light for improved dye degradation and antimicrobial activity, Epub Print. (21 June 2024), https://doi.org/10.21203/rs.3.rs-4549219/v1.
[16] G. Demircan, S. Yalcin, K. Alivi, et al., The effect of Co and Mn Co-Doping on structural and optical properties of ZnO thin films, Opt. Mater. (Amst.) 126 (April 2022), https://doi.org/10.1016/j.optmat.2022.112163.
[17] R.F. Herin, A.S.S. Judit, S. Sebastiammal, et al., Functionalized ZnO NPs and Biopolymers-Coated ZnO NPs for Drug Delivery and Biomedical Applications—A Review, Regen. Eng. Transl. Med. 11 (2025) 165–189.
[18] V. Harish, D. Tewari, M. Gaur, et al., Review on Nanoparticles and Nanostructured Materials: Bioimaging, Biosensing, Drug Delivery, Tissue Engineering, Antimicrobial, and Agro-Food Applications, Nanomaterials 12 (February 2022), https://doi.org/10.3390/nano12030457.
[19] E.B. Buzok, S. Yalcin, G. Demircan, et al., Effect of a cobalt complex on the structural, optical, electrical, and anti-reflective properties of ZnO thin films, Ceram. Int. 51 (2025) 38702–38711.
[20] L. Hu, M. Xing, X. He, et al., Photocatalytic degradation of tetracycline hydrochloride by ZnO/TiO2 composite photocatalyst, Journal Materials Science Materials Electronics 34 (December 2023), https://doi.org/10.1007/s10854-023-11690-2.
[21] E.B. Buzok, S. Yalcin, G. Demircan, et al., The structural, optical, electrical and radiation shielding properties of Co-doped ZnO thin films, Radiat. Phys. Chem. 222 (September 2024), https://doi.org/10.1016/j.radphyschem.2024.111840.
[22] S. Subramanian, K. Neyvasagam, S.S. kumar, et al., Room-temperature ammonia gas sensor based on Ti-doped ZnO thin films prepared via wet chemical synthesis using drop casting technique, Sens. Actuators A Phys. 387 (June 2025), https://doi.org/10.1016/j.sna.2025.116396.
[23] E. Aslan, M. Zarbali, Highly sensitive zinc oxide ultraviolet photodetector by titanium incorporation, Thin Solid. Films 724 (April 2021), https://doi.org/10.1016/j.tsf.2021.138627. Epub ahead of print 30.
[24] G. Demircan, A. Acikgoz, S. Yalcin, et al., The Influence of Doping Perimidine Ruthenium Complexes on Structural, Optic, and Residual Stress Properties of ZnO Thin Films, Braz. J. Phys. 53 (1) (February 2023), https://doi.org/10.1007/s13538-022-01245-x.
[25] M. Cesaria, B.Di Bartolo, Nanophosphors-based white light sources, Nanomaterials 9 (July 2019), https://doi.org/10.3390/nano9071048.
[26] R. Sarathi, N.L. Sheeba, E. Selva Essaki, et al., Titanium doped Zinc Oxide nanoparticles: A study of structural and optical properties for photocatalytic applications. Materials Today: Proceedings, Elsevier Ltd, 2022, pp. 1859–1863.
[27] Aneesh P.M., Jayaraj M.K. Red luminescence from hydrothermally synthesized Eu-doped ZnO nanoparticles under visible excitation. 2010.
[28] V.V. Manju, R. Sanjana, V.N. Hegde, et al., Structural, morphological, optical, and electromechanical analysis of green-synthesized Ti-doped ZnO nanoparticles for optoelectronic applications, Micro Nanostruct. 211 (March 2026), https://doi.org/10.1016/j.micrna.2025.208537.
[29] E. Aslan, M. Zarbali, Tuning of photosensitivity and optical parameters of ZnO based photodetectors by co-Sn and Ti doping, Opt. Mater. 125 (March 2022), https://doi.org/10.1016/j.optmat.2022.112030.
[30] R. Kubrin, Nanophosphor coatings: technology and applications, opportunities and challenges, KONA Powder Part. J. 31 (2014) 22–52.
[31] H.S. Han, J.U. Jang, D. Oh, et al., Advances and perspectives of titanium-based nanocomposites for energy generation and environmental remediation applications: a review, Energy Fuels 37 (2023) 17708–17735.

[32] D. Wang, R. Su, H. Li, et al., Effect of Ti content on the strengthening and fracture damage mechanism of mechanical properties of weathering steel, J. Mater. Res. Technol. 30 (2024) 3690–3704.
[33] R. Ade, S.S. Kumar, S. Valanarasu, et al., Enhanced optoelectronic properties of Ti-doped ZnO nanorods for photodetector applications, Ceram. Int. 47 (2021) 24031–24038.
[34] M.L. Lee, J.C. Wang, C.H. Kao, et al., Comparison of ZnO and Ti-doped ZnO sensing membrane applied in electrolyte-insulator-semiconductor structure, Ceram. Int. 44 (2018) 6081–6088.
[35] D. Singh, V.S. Kundu, A.S. Maan, Structural, morphological and gas sensing study of zinc doped tin oxide nanoparticles synthesized via hydrothermal technique, J. Mol. Struct. 1115 (2016) 250–257.
[36] S. Suthakaran, S. Dhanapandian, N. Krishnakumar, et al., Hydrothermal synthesis of surfactant assisted Zn doped SnO2 nanoparticles with enhanced photocatalytic performance and energy storage performance, J. Phys. Chem. Solids 141 (June 2020), https://doi.org/10.1016/j.jpcs.2020.109407.
[37] H. Ibrahim, M. Abdel-Rahman, H. Khallaf, et al., A Study of Ti Incorporation in ZnO Nanoflakes Synthesized by Citrate Route Method, J. Nanotechnol. Adv. Mater. 12 (2024) 1–11.
[38] S. Suresh, B. Subash, S. Karthikeyan, Electrical, optical and photocatalytic properties of Ti-loaded ZnO/ZnO and Ti-loaded ZnO nanospheres, J. Iran. Chem. Soc. 14 (2017) 1591–1600.
[39] I. Darmadi, A. Taufik, R. Saleh, Analysis of optical and structural properties of Ti-doped ZnO nanoparticles synthesized by co-precipitation method. Journal of Physics: Conference Series, Institute of Physics Publishing, 2020, https://doi.org/10.1088/1742-6596/1442/1/012021.
[40] Q. Huo, X. Meng, J. Ma, et al., Photoluminescence and energy transfer properties of Eu3+, Mn4+-activated perovskite LaTiO3 phosphors, 5, J. Alloy. Compd. 1050 (January 2026), https://doi.org/10.1016/j.jallcom.2025.185858, 5.
[41] A. Olori, D. Pietro, A. Campopiano, Preparation of ultrapure kbr pellet: new method for FTIR quantitative analysis, Int. J. Sci. Acad. Res. 02 (2021) 1015–1020.
[42] B. Sumalatha, C. Rajyasree, K.V. Pavana Kumari, et al., Structural, Optical and Morphological Studies of TiO2 Incorporated MgZn2(PO4)2 Nanophosphors by Solid-state Reaction, Phys. Chem. Res. 13 (2025) 755–766.
[43] L. Escobar-Alarcón, P.R. Gonzalez-Martinez, S. Romero, et al., Thermoluminescent response of Zn-modified titanium dioxide thin films subjected to continuous or pulsed ultraviolet radiation, Appl. Radiat. Isot. 226 (December 2025), https://doi.org/10.1016/j.apradiso.2025.112111.
[44] B. Pant, G.P. Ojha, Y.S. Kuk, et al., Synthesis and characterization of zno-tio2/carbon fiber composite with enhanced photocatalytic properties, Nanomaterials 10 (2020) 1–12.
[45] R. Marsalek, Particle Size and Zeta Potential of ZnO, APCBEE Procedia 9 (2014) 13–17.
[46] S. Sahoo, M. Maiti, A. Ganguly, et al., Effect of zinc oxide nanoparticles as cure activator on the properties of natural rubber and nitrile rubber, J. Appl. Polym. Sci. 105 (2007) 2407–2415.
[47] M. Serhan, M. Sprowls, D. Jackemeyer, et al., Total iron measurement in human serum with a smartphone. AIChE Annual Meeting, Conference Proceedings, American Institute of Chemical Engineers, 2019, https://doi.org/10.1039/x0xx00000x.
[48] D. Fang, F. He, J. Xie, et al., Calibration of Binding Energy Positions with C1s for XPS Results, J. Wuhan. Univ. Technol. Mater. Sci. Ed. 35 (2020) 711–718.
[49] A. Ali, Y.W. Chiang, R.M. Santos, X-Ray Diffraction Techniques for Mineral Characterization: A Review for Engineers of the Fundamentals, Applications, and Research Directions, Minerals 12 (February 2022), https://doi.org/10.3390/min12020205.
[50] S.A. Bidier, M.R. Hashim, A.M. Al-Diabat, et al., Effect of growth time on Ti-doped ZnO nanorods prepared by low-temperature chemical bath deposition, Phys. E Low. Dimens. Syst. Nanostruct. 88 (2017) 169–173.
[51] K. Mattsson, S. Jocic, J.A. de Lima, et al., Nanoplastics in aquatic environments—Sources, sampling techniques, and identification methods. Microplastic Contamination in Aquatic Environments: An Emerging Matter of Environmental Urgency, Elsevier, 2023, pp. 381–397.
[52] T. Sun, H. Hao, W. ting Hao, et al., Preparation and antibacterial properties of titanium-doped ZnO from different zinc salts, Nanoscale Res. Lett. 9 (2014) 1–11.
[53] P. Raji, K.B. Kumar, Investigation of Ti doping on the structural, optical, and magnetic properties of ZnO nanoparticles, Journal Materials Science Materials Electronics 32 (2021) 11751–11762.
[54] G. Barsisa, A. Belay, G. Beyene, et al., Synthesis Europium (Eu3+) Doped Zinc Oxide Nanoparticles via the Co-Precipitation Method for Photocatalytic Applications, Nano Biomed. Eng. 14 (2022) 58–70.
[55] S.A. Bidier, M.R. Hashim, M. Bououdina, Structural and optical characteristics of Ti-doped ZnO nanorods deposited by simple chemical bath deposition, J. Mater. Sci. Mater. Electron. 28 (2017) 11178–11185.
[56] M. Rafique, R. Tahir, N.R. Khalid, et al., Hydrothermal synthesis of an efficient and visible light responsive pure and strontium doped zinc oxide nano-hexagonal photocatalysts for photodegradation of Rhodamine B dye, Appl. Nanosci. (Switz.) 11 (2021) 1045–1056.
[57] S. Singh, J.V. Gade, D.K. Verma, et al., Exploring ZnO nanoparticles: UV–visible analysis and different size estimation methods, Opt. Mater. (Amst.) 152 (June 2024), https://doi.org/10.1016/j.optmat.2024.115422.
[58] M. Yuste, R. Escobar-Galindo, N. Benito, et al., Effect of the incorporation of titanium on the optical properties of zno thin films: From doping to mixed oxide formation, Coatings 9 (2019), https://doi.org/10.3390/coatings9030180.
[59] P.H.M. Andrade, C. Volkringer, T. Loiseau, et al., Band gap analysis in MOF materials: Distinguishing direct and indirect transitions using UV–vis spectroscopy, Appl. Mater. Today 37 (April 2024), https://doi.org/10.1016/j.apmt.2024.102094.
[60] K.P. Sridevi, L. Guru Prasad, B. Sangeetha, et al., Structural and optical study of ZnO-TiO2 nanocomposites, J. Ovonic Res. 18 (2022) 453–464.
[61] A. Bhattacharyya, R. Dash, Intrinsic defects formation and subsequent direct and indirect transitions due to ammonia in rGO – ZnO nanocomposites, Adv. Mater. Proc. (January 2023), https://doi.org/10.5185/amp.2023.6186.1007.
[62] P.P. Ortega, J.V.N. Palma, A.L. Doimo, et al., Influence of Different Synthesis Methods on the Defect Structure, Morphology, and UV-Assisted Ozone Sensing Properties of Zinc Oxide Nanoplates, Chemosensors 13 (April 2025), https://doi.org/10.3390/chemosensors13040152.
[63] R. Krishna, P.K. Yadaw, V. Dubey, et al., Instrumentation techniques for radiation dosimetry by using luminescence spectroscopy techniques. In: *Rare-Earth-Activated Phosphors: Chemistry and Applications*, Elsevier, 2022, pp. 43–67.
[64] M. Kubas, H.Y. Salah, A. El-Shaer, et al., Investigating the impact of different growth temperatures on the photoelectrochemical, and optical properties of zinc oxide nanorod for electrical and optoelectronic applications, Sci. Rep. 16 (1) (December 2026), https://doi.org/10.1038/s41598-025-26341-1.
[65] M. Nistor, D. Dobrin, F. Gherendi, et al., Impact of high oxygen deficiency on the photoluminescence properties of black zinc oxide thin films, Nanoscale 17 (2025) 23000–23009.
[66] A. Hassan, A.A. Khan, Y.H. Ahn, et al., Orientation-Mediated Luminescence Enhancement and Spin-Orbit Coupling in ZnO Single Crystals, Nanomaterials 12 (July 2022), https://doi.org/10.3390/nano12132192.
[67] K. Safeen, A. Safeen, D. Arif, et al., Tuning the Optical Properties of ZnO by Co and Gd Doping for Water Pollutant Elimination, Water (Switz.) 15 (April 2023), https://doi.org/10.3390/w15081470.
[68] M. Gasztych, A. Malamis, W. Musiał, The Influence of Initiators, Particle Size and Composition on the Electrokinetic Potential of N-(Isopropyl)acrylamide Derivatives, Polymers 16 (April 2024), https://doi.org/10.3390/polym16070907.
[69] J. Rodriguez-Loya, M. Lerma, J.L. Gardea-Torresdey, Dynamic light scattering and its application to control nanoparticle aggregation in colloidal systems: a review, Micromachines 15 (January 2024), https://doi.org/10.3390/mi15010024.
[70] A.M.M. Tamboli, J. Munaf Tade, Zeta Potential: A Comprehensive Review, Int. Res. J. Pharm. Med. Sci. (IRJPMS 8 (2025) 115–124.
[71] S. Kamble, S. Agrawal, S. Cherumukkil, et al., Revisiting Zeta Potential, the Key Feature of Interfacial Phenomena, with Applications and Recent Advancements, 1, ChemistrySelect 7 (January 2022), https://doi.org/10.1002/slct.202103084, 1.
[72] M.M. Modena, B. Rühle, T.P. Burg, et al., Nanoparticle Characterization: What to Measure? Adv. Mater. 31 (2019) https://doi.org/10.1002/adma.201901556.
[73] W. Wan, J. Su, X.D. Zou, et al., Transmission electron microscopy as an important tool for characterization of zeolite structures, Inorg. Chem. Front. 5 (2018) 2836–2855.
[74] Z. Wan, W.S. Kwack, W.J. Lee, et al., Electrical and optical properties of Ti doped ZnO films grown on glass substrate by atomic layer deposition, Mater. Res. Bull. 57 (2014) 23–28.
[75] M. Anwar, M.A.S. Abdul, U.M. Khan, et al., A review of X-ray photoelectron spectroscopy technique to analyze the stability and degradation mechanism of solid oxide fuel cell cathode materials, Materials 15 (April 2022), https://doi.org/10.3390/ma15072540.
[76] F. Orudzhev, M. Gadzhiev, M. Abdulkerimov, et al., Plasma-Assisted Synthesis of TiO2/ZnO Heterocomposite Microparticles: Phase Composition, Surface Chemistry, and Photocatalytic Performance, Molecules 30 (August 2025), https://doi.org/10.3390/molecules30163371.
[77] N.M. Hosny, I. Gomaa, M.G. Elmahgary, et al., ZnO doped C: Facile synthesis, characterization and photocatalytic degradation of dyes, Sci. Rep. 13 (1) (December 2023), https://doi.org/10.1038/s41598-023-41106-4.
[78] M. Tomić, M. Claros, I. Gràcia, et al., Zno structures with surface nanoscale interfaces formed by au, fe2o3, or cu2o modifier nanoparticles: Characterization and gas sensing properties, Sensors 21 (July 2021), https://doi.org/10.3390/s21134509.
[79] R. Ramadan, D. Romera, R.D. Carrascon, et al., Sol−gel-deposited Ti-doped ZnO: Toward cell fouling transparent conductive oxides, ACS Omega 4 (2019) 11354–11363.
[80] B. Bharti, S. Kumar, H.N. Lee, et al., Formation of oxygen vacancies and Ti3+ state in TiO2 thin film and enhanced optical properties by air plasma treatment, Sci. Rep. 6 (August 2016), https://doi.org/10.1038/srep32355. Epub ahead of print 30.